energies

*Article*

# Classification and Assessment of Core Fractures in a Post-Fracturing Conglomerate Reservoir Using the AHP–FCE Method

**Renyan Zhuo [1], Xinfang Ma [1,*], Shicheng Zhang [1], Junxiu Ma [2], Yuankai Xiang [2] and Haoran Sun [2]**

[1] State Key Laboratory of Petroleum Resources and Prospecting, China University of Petroleum-Beijing, Beijing 102249, China
[2] Engineering Technology Research Institute, PetroChina Xinjiang Oilfield Company, Karamay 834000, China
* Correspondence: maxinfang@cup.edu.cn

**Abstract:** To characterize the hydraulic fracture network of a conglomerate reservoir, a slant core well was drilled aimed to obtain direct information regarding hydraulic fractures through slant core at the conglomerate hydraulic fracturing test site (CHFTS). Core fracture classification was the fundamental issue of the project. In this study, three grade classifications for core fractures were proposed. Comprehensive classification of core fractures was carried out using the analytic hierarchy process (AHP)–fuzzy comprehensive evaluation (FCE) method. Finally, the fracture classification results were validated against numerical simulation. The grade-1 fracture classification included hydraulic fractures, drilling-induced fractures and core cutting-induced fractures. A total of 214 hydraulic fractures were observed. For the grade-2 classification, the hydraulic fractures were divided into 47 tensile fractures and 167 shear fractures. For the grade-3 classification, the shear fractures were subdivided into 45 tensile-shear fractures and 122 compression-shear fractures. Based on the numerical verification of the core fracture classifications, the dataset acquired was applied to analyze the spatial distribution of tensile and shear fractures. Results showed that the tensile fractures were mainly in the near-wellbore area with lateral distances of less than 20–25 m from the wellbore. The shear fractures were mainly in the far-wellbore area with lateral distances of 20–30 m from the wellbore. These results provide a basis for understanding the fracture types, density, and failure mechanisms of post-fracturing conglomerate reservoir.

**Keywords:** CHFTS; slant core well; fracture classification; analytical hierarchy process (AHP); fuzzy comprehensive evaluation (FCE)

check for updates

**Citation:** Zhuo, R.; Ma, X.; Zhang, S.; Ma, J.; Xiang, Y.; Sun, H. Classification and Assessment of Core Fractures in a Post-Fracturing Conglomerate Reservoir Using the AHP–FCE Method. *Energies* **2023**, *16*, 418. https://doi.org/10.3390/en16010418

Academic Editor: Xinpu Shen

Received: 5 December 2022
Revised: 24 December 2022
Accepted: 27 December 2022
Published: 29 December 2022

**Copyright:** © 2022 by the authors. Licensee MDPI, Basel, Switzerland. This article is an open access article distributed under the terms and conditions of the Creative Commons Attribution (CC BY) license (https://creativecommons.org/licenses/by/4.0/).

## 1. Introduction

The development of a large conglomerate reservoir of Mahu depression in the Junggar basin has attracted extensive attention. The conglomerate formation is tight and heterogeneous [1]. Therefore, only relying on geophysical logging analysis or a single mechanical test cannot meet the requirements of reservoir fracture geometry analysis [2,3]. In particular, irregular conglomerate particles have significant influences on fracture propagation behavior. Many scholars have carried out substantial numerical simulations and experimental research regarding the propagation of hydraulic fractures in conglomerate. Xv et al. [4] found that under laboratory conditions, most fractures extend via bypassing the gravel pattern under small displacement and fractures extend via through-penetrating gravel pattern under large displacement. Liu et al. [5] found that when the horizontal geostress ratio is lower than 1:1.7, multiple fractures occur and propagate via bypassing gravel pattern. Yu et al. [6] noted that slick-water fracturing tends to form multiple fractures. Guar gum fracturing tends to form bypassing gravel double-wing fractures. To clarify the extension mechanism of hydraulic fracture, Dong et al. [7] proposed that the hydraulic fracture extension and the fluid front have different velocities, and that the fluid front will

lag behind the crack tip. Shentu et al. [8] investigated the fracture propagation mechanism in a conglomerate reservoir using the discrete element method, which showed that the through-penetrating gravel pattern occurs when the strength of conglomerate gravels is relatively low; otherwise, the bypassing gravel pattern occurs. Liang et al. [9] simulated hydraulic fracturing in a conglomerate reservoir at lab scale using a cohesive zone model; their results indicated that gravel particles could reduce the rate of fracture propagation and cause path bending.

The existing fracture identification process primarily focuses on the characterization of natural fractures of unfractured formations. Formation image logs and seismic datasets have been the major sources of fracture identification; applied fracture identification methods have included deep learning [10], big data analytics [11], multi-waveform classification and seismic attributes analysis [12]. However, these technologies can only interpret fractures; they cannot further identify the fracture type.

The fracture propagation patterns and extension mechanisms of conglomerate reservoirs have been studied through physical experiments and numerical simulation, and a general understanding has been obtained. However, this understanding does not extend to hydraulic fractures under in situ conditions, and the hydraulic fracture density, type and propagation mechanism are still not well understood. For fracture classification, scholars have carried out many studies of HFTS1 [13,14] and HFTS2 [15–17]. According to core fracture observation, the slant core fractures were mainly divided into three types (hydraulic fractures, natural fractures and induced fractures) without further subdivision of hydraulic fractures. There is no clear method to identify core fracture types.

In this study, the objective was to identify the core fractures in a post-fracturing conglomerate reservoir. Understanding the density, geometry and propagation mechanism of hydraulic fractures was a new field. Based on the cores drilled at the CHFTS, the core fracture description, FIM image logging and core CT scans were combined to determine the core fracture classification index. The AHP–FCE was adopted as the fracture identification method in the conglomerate reservoir. The validated dataset was used to further assess the formation mechanism of tensile and shear fractures.

## 2. CHFTS Overview

The CHFTS is a hydraulic fracturing test site located in the Junggar basin. Figure 1 shows a plan view of the slant core well trajectory and the adjacent producing horizontal wells. The test site contains twelve producing horizontal wells and a slant core well referred to as S1. Seven adjacent horizontal wells were drilled in the upper $T_1b_3$ formation and five wells were drilled in the lower $T_1b_2$ formation. The slant core well (S1) was drilled from northwest to southeast with an azimuth of 175.0° and an angle of inclination of 80.3°. The first cored interval recovered 194.95 m of core involving the fractures of wells H8/H9 in the $T_1b_3$, and the second cored interval recovered 98.76 m of core involving the fractures of well H4 in the $T_1b_2$.

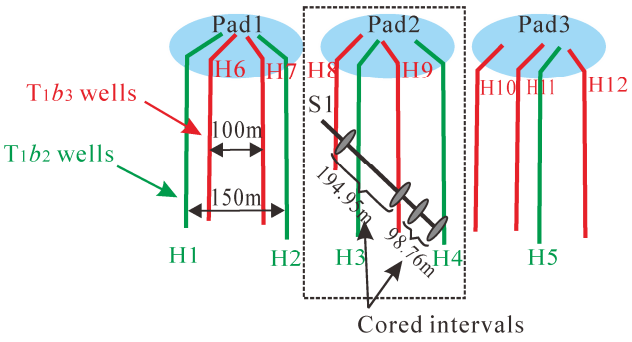



**Figure 1.** Plan view of twelve horizontal wells and the slant core well in the CHFTS. The slant core well is in black, and goes through the fractures of H8/H9 in the $T_1b_3$ and H4 in the $T_1b_2$.

## 3. Core Fracture Classification Indexes

According to the causes of the core fractures, they were divided into hydraulic fractures (HF), drilling-induced fractures (DF), and core cutting-induced fractures (CF). In this study, we focused on the identification of hydraulic fractures. Next, based on fracture characteristics under different mechanical states, hydraulic fractures were subdivided into tensile fractures (TF) and shear fractures (SF). Shear fractures were subdivided into tensile-shear fractures (T-SF) and compression-shear fractures (C-SF).

The core fracture descriptions, FIM image logging and core CT scans were combined to systematically study the characteristics of core fractures, summarized as follows.

### *3.1. Hydraulic Fracture (HF)*

Figure 2 shows the features of a hydraulic fracture; the fracture morphology features contain straight, microwave and crushed zones [18]. The fracture profile is incomplete and mostly gravel scattered. The fracture surfaces have through-penetrating gravel and bypassing gravel patterns. The fractures are filled with materials including mud and proppant. Combined with FIM imaging logging, most hydraulic fractures are high angle fractures and high conductivity fractures.

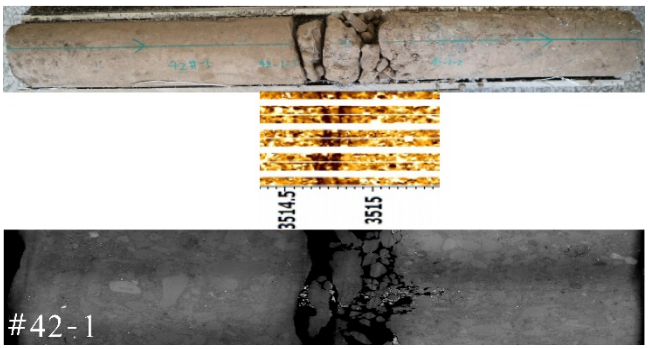



**Figure 2.** Features of a hydraulic fracture.

The hydraulic fractures were subdivided into tensile fractures and shear fractures. As demonstrated in Figure 3, tensile fractures had large apertures and bypassing gravel surfaces.

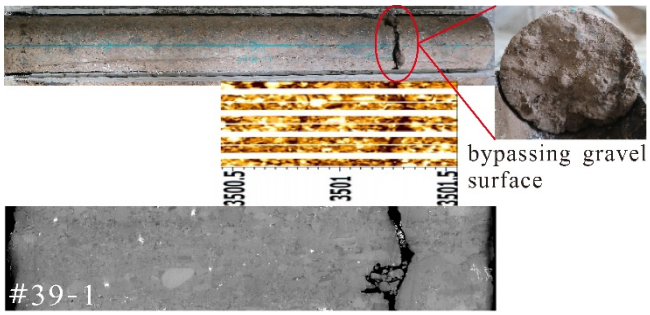



**Figure 3.** Features of a tensile fracture.

In contrast, shear fractures had small apertures and through-penetrating gravel surfaces, as shown in Figure 4.

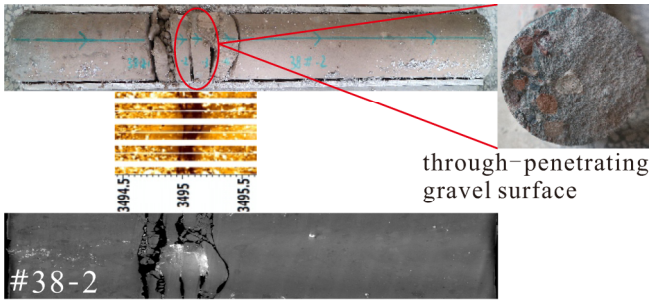



**Figure 4.** Features of a shear fracture.

Slight differences were found in the characteristics of shear fractures. Next, the shear fractures were subdivided into tensile-shear fractures and compression-shear fractures. Compared with compression-shear fractures, tensile-shear fractures had rougher fracture surfaces and larger apertures (shown in Figure 5). In particular, compression-shear fractures had crushing traces in morphology (shown in Figure 6).

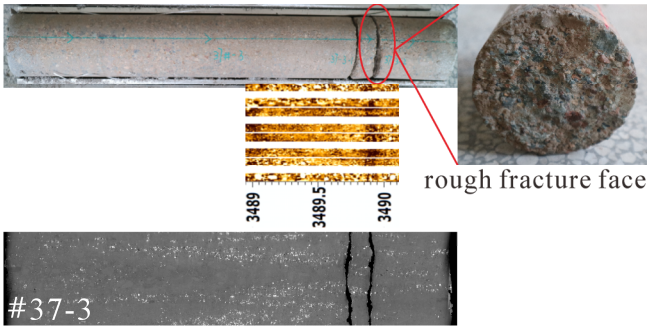



**Figure 5.** Features of a tensile-shear fracture.

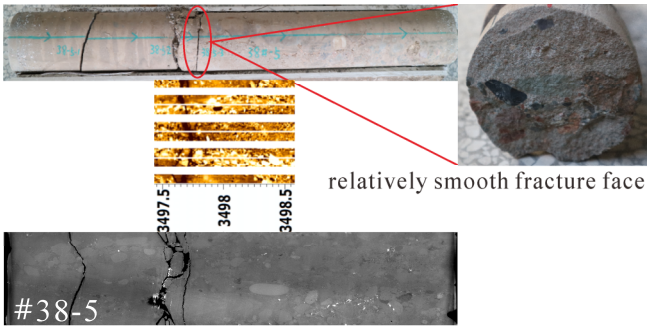



**Figure 6.** Features of a compression-shear fracture.

### *3.2. Drilling-Induced Fracture (DF)*

A drilling-induced fracture is shown in Figure 7. The fracture is irregular serrated or microwave in morphology, and the fracture profile is complete. The fracture surfaces have a bypassing gravel feature with an uneven small amount of mud adhesion. Drilling-induced fractures of the cores could not be observed in FIM imaging logging, but could be observed in core CT scans.




**Figure 7.** Features of a drilling-induced fracture.

### *3.3. Core Cutting-Induced Fracture (CF)*

A core cutting-induced fracture is shown in Figure 8. The fracture is irregular serrated in morphology, and the fracture profile is complete. The fracture surfaces have a bypassing gravel feature with no mud adhesion. Core cutting-induced fractures could not be observed in FIM imaging logging or core CT scans.



**Figure 8.** Features of a core cutting-induced fracture.

Based on the data set, including core fracture description characteristics, FIM imaging logging and core CT scans, the fracture classification indexes were determined; the indexes include fracture morphology, fracture integrity, fracture surface feature, fracture surface roughness, fracture filling, fracture aperture, fracture interpreted by FIM image logging and proppant in core CT scans, as shown in Table 1.

**Table 1.** Table of fracture classification indexes.

| Classification Indexes | | Fracture Types | | | | |
|---|---|---|---|---|---|---|
| **One-Level Indexes** | **Two-Level Indexes** | **Tensile Fracture** | **Tensile-Shear Fracture** | **Compression-Shear Fracture** | **Drilling-Induced Fracture** | **Core Cutting-Induced Fracture** |
| Core fracture description | Fracture morphology | Microwave | Microwave or Crushed zone | Straight or Crushed zone | Serrate | Serrate |
| | Fracture integrity | Incomplete | Incomplete or Partially-complete | Incomplete or Partially-complete | Complete | Complete |
| | Fracture surface feature | Bypassing gravel | Through-penetrating gravel | Through-penetrating gravel | Bypassing gravel | Bypassing gravel |
| | Fracture surface roughness | Rough | Rough | Relatively smooth | Rough | Rough |
| | Fracture filling | Mineral deposits or drilling mud | Mineral deposits or drilling mud | Drilling mud | Uneven mud | No |
| | Fracture aperture (cm) | $\geq$0.5 | $\geq$0.5 | <0.5 | <0.5 | <0.5 |
| FIM imaging logging | Fracture interpreted by FIM | Yes | Yes | Yes or no | No | No |
| Core CT scans | Proppant | Yes or no | Yes or no | Yes or no | No | No |

## 4. AHP–FCE Method of Core Fracture Identification

### *4.1. Index Weight of Index Determination Using AHP*

The analytic hierarchy process (AHP)–fuzzy comprehensive evaluation (FCE) method was adopted to identify core fractures.

First, based on the eight fracture classification indexes, a hierarchical structure model of core fracture identification was established, as shown in Figure 9.

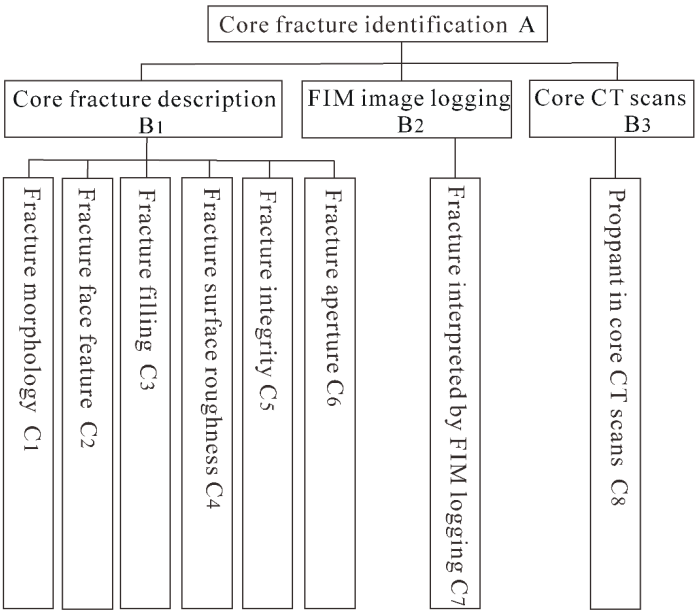



**Figure 9.** Hierarchical structure model of core fracture identification.

Next, the index weight of ordering in a single level was determined using the AHP [19,20] as follows. The judgment matrix was set up with the adoption of the "ninth level method". The maximum eigenvalue ($\lambda_{max}$) and its eigenvector ($W_i$) were calculated using the square root method, with $W_i$ as each index weight, as shown in Table 2. In Table 2, the row of judgment matrix is $n$, which is the number of indexes in each level of the sub-hierarchy; the judgment matrix is $A$, and $AW$ is the vector obtained as multiplying $A$ by $W$.

**Table 2.** A-B index weight using the square root method.

| A | $B_1$ | $B_2$ | $B_3$ | $M=\prod M_{ij}$ | $W_i'=\sqrt[n]{M}$ | $W_i=W_i'/\sum W_i'$ | $(AW)_i$ | $(AW)_i/W_i$ |
|---|---|---|---|---|---|---|---|---|
| $B_1$ | 1 | 2 | 3 | 1.8171 | 0.5396 | 0.5396 | 1.6238 | 3.0092 |
| $B_2$ | 1/2 | 1 | 2 | 1.0000 | 0.2970 | 0.2970 | 0.8936 | 3.0092 |
| $B_3$ | 1/3 | 1/2 | 1 | 0.5503 | 0.1634 | 0.1634 | 0.4918 | 3.0092 |
| - | - | - | - | Total | 1 | 1 | - | 9.0276 |

From Table 2, the index weight of the core fracture description ($B_1$), FIM imaging logging ($B_2$) and core CT scans ($B_3$) are: $W^{A-B} = (0.5396,\ 0.2970,\ 0.1634)$, respectively.

Finally, a consistency index was used to test the consistency of ordering in single level. Using the square root method, the maximum eigenvalue was obtained, as shown in the following equation:

$$\lambda_{max} = \frac{1}{n}\sum_{i=1}^{n}\frac{(AW)_i}{W_i} = \frac{1}{3} \times 9.0276 = 3.0092 \quad (1)$$

The consistency index is:

$$CI = \frac{\lambda_{max}}{n-1} = \frac{3.0092-3}{3-1} = 0.0046 \quad (2)$$

The consistency ratio is:

$$CR = \frac{CI}{RI} = \frac{0.0046}{0.58} = 0.0079 \quad (3)$$

*RI* is the average random consistency index; the values of *RI* are presented in Table 3. The judgment matrix is satisfactory when $CR \leq 0.1$.

**Table 3.** Values of the average random consistency index.

| *n* | 1 | 2 | 3 | 4 | 5 | 6 | 7 | 8 | 9 |
|---|---|---|---|---|---|---|---|---|---|
| *RI* | 0.00 | 0.00 | 0.58 | 0.90 | 0.12 | 1.24 | 1.32 | 1.41 | 1.45 |

Similarly, each index in sub-principle can be ordered in single level, and index weight can be determined. The index weights of $B_1$ are: $W^{B1-C} = (0.3246, 0.1137, 0.2256, 0.0553, 0.2256, 0.0553)$. The consistency ratio is 0.0311, which is less than 0.1; therefore, the judgment matrix is satisfactory. The index weights of core fracture identification are $W = (0.1752, 0.0614, 0.1217, 0.0298, 0.1217, 0.0298, 0.2970, 0.1634)$, as shown in Table 4.

**Table 4.** Index weights of core fracture identification indexes.

| One-Level Indexes | Two-Level Indexes | $W^{A-B}$ | $W^{B-C}$ | $W$ |
|---|---|---|---|---|
| $B_1$ | $C_1$ | 0.5396 | 0.3246 | 0.1752 |
| | $C_2$ | | 0.1137 | 0.0614 |
| | $C_3$ | | 0.2256 | 0.1217 |
| | $C_4$ | | 0.0553 | 0.0298 |
| | $C_5$ | | 0.2256 | 0.1217 |
| | $C_6$ | | 0.0553 | 0.0298 |
| $B_2$ | $C_7$ | 0.2970 | 1 | 0.2970 |
| $B_3$ | $C_8$ | 0.1634 | 1 | 0.1634 |

### *4.2. Core Fracture Type Confirmation Using FCE*

On the basis of the AHP calculation of index weight, the core fracture type was assessed using the fuzzy comprehensive evaluation (FCE) method [19], as described in the following 3 steps.

(1) Create a single-index fuzzy evaluation matrix. According to practical experience or expert evaluation, a fuzzy mapping can be obtained from the indexes set to the evaluation set; it expresses the membership grade of an index to fracture types.
(2) Construct a fuzzy evaluation matrix for a single fracture. According to experts' judgment of a fracture, obtain the membership grade of each characteristic index of the fracture to the fracture types, as shown in Table 5.

**Table 5.** Fuzzy evaluation of a single fracture.

| Indexes | Value of Indexes | Fuzzy Evaluation Matrix |
|---|---|---|
| $C_1$ | Microwave | $u^{(1)}$ = (0.4, 0.4, 0.2, 0, 0) |
| $C_2$ | Incomplete | $u^{(2)}$ = (0.4, 0.4, 0.2, 0, 0) |
| $C_3$ | Bypassing gravel | $u^{(3)}$ = (0.4, 0, 0, 0.3, 0.3) |
| $C_4$ | Rough | $u^{(4)}$ = (0.25, 0.15, 0.1, 0.25, 0.25) |
| $C_5$ | Drilling mud | $u^{(5)}$ = (0.3, 0.3, 0.3, 0.1, 0) |
| $C_6$ | ≥0.5 | $u^{(6)}$ = (0.4, 0.4, 0.2, 0, 0) |
| $C_7$ | Yes | $u^{(7)}$ = (0.33, 0.33, 0.34, 0, 0) |
| $C_8$ | No | $u^{(8)}$ = (0.2, 0.2, 0.2, 0.2, 0.2) |

From Table 5, a fuzzy evaluation matrix is obtained; it is defined as $R$:

$$R = \left(u^{(1)},\ u^{(2)},\ u^{(3)},\ u^{(4)},\ u^{(5)},\ u^{(6)},\ u^{(7)},\ u^{(8)}\right)^{\mathrm{T}} = \begin{bmatrix} 0.4 & 0.4 & 0.2 & 0 & 0 \\ 0.4 & 0.4 & 0.2 & 0 & 0 \\ 0.4 & 0 & 0 & 0.3 & 0.3 \\ 0.25 & 0.15 & 0.1 & 0.25 & 0.25 \\ 0.3 & 0.3 & 0.3 & 0.1 & 0 \\ 0.4 & 0.4 & 0.2 & 0 & 0 \\ 0.33 & 0.33 & 0.34 & 0 & 0 \\ 0.2 & 0.2 & 0.2 & 0.2 & 0.2 \end{bmatrix} \quad (4)$$

(3) Calculate the fuzzy evaluation set. The fuzzy evaluation set ($B$) is calculated by multiplying the index weight $W$ and the fuzzy evaluation matrix $R$, as follows:

$$B = W \times R = (0.1752, 0.0614,\ 0.1217,\ 0.0298,\ 0.1217,\ 0.0298,\ 0.2970,\ 0.1634) \times \begin{bmatrix} 0.4 & 0.4 & 0.2 & 0 & 0 \\ 0.4 & 0.4 & 0.2 & 0 & 0 \\ 0.4 & 0 & 0 & 0.3 & 0.3 \\ 0.25 & 0.15 & 0.1 & 0.25 & 0.25 \\ 0.3 & 0.3 & 0.3 & 0.1 & 0 \\ 0.4 & 0.4 & 0.2 & 0 & 0 \\ 0.33 & 0.33 & 0.34 & 0 & 0 \\ 0.2 & 0.2 & 0.2 & 0.2 & 0.2 \end{bmatrix} = \begin{bmatrix} 0.3299 & 0.2782 & 0.2264 & 0.0888 & 0.0766 \end{bmatrix} \quad (5)$$

The fuzzy evaluation set $B$ indicates that the membership grade to tensile fracture is 0.3299, to tensile-shear fracture is 0.2782, to compression-shear fracture is 0.2264, to drilling-induced fracture is 0.0888, and to core cutting-induced fracture is 0.0766. Referring to the max-subjection principle, this fracture was identified as a tensile fracture.

## 5. Core Fracture Classification Results and Verification

Figure 10 shows the core fractures along the coring trajectory. In 293.71 m cores, for grade-1 fracture classification, approximately 214 hydraulic fractures, 90 drilling-induced fractures and 48 core cutting-induced fractures were identified. For grade-2 classification, hydraulic fractures were divided into 47 tensile fractures and 167 shear fractures. For grade-3 classification, shear fractures were subdivided into 45 tensile-shear fractures and 122 compression-shear fractures. Vertically, the hydraulic fractures in the cores were distributed in the range of 11.5 m above and 14.6 m below the wellbores of the adjacent producing horizontal wells. Horizontally, hydraulic fractures propagated within 100 m from the well spacing, as shown in Figure 11.

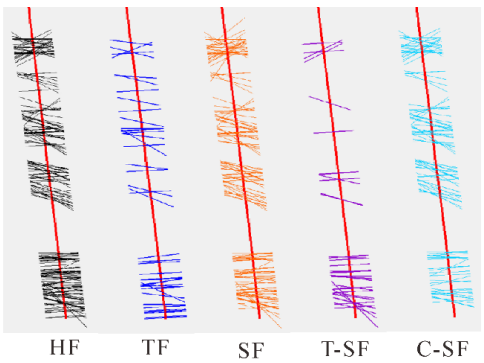



**Figure 10.** Core fractures along the coring trajectory.

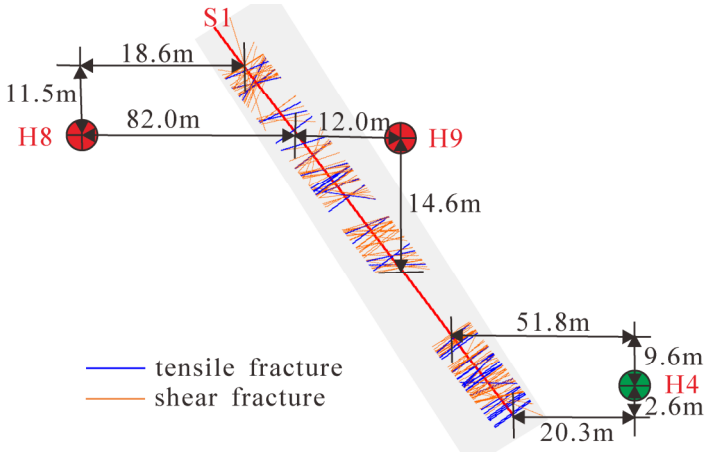



**Figure 11.** Diagram of hydraulic fractures along the coring trajectory with respect to the adjacent horizontal wells.

According to the principle of minimum lateral distance, the fractures were mapped to adjacent horizontal wells. Based on this, the distribution of fracture density in the cored intervals with respect to the lateral distance from the adjacent horizontal wellbores was analyzed, as shown as Figures 12 and 13. It was concluded that in the near-wellbore area with lateral distances less than 20–25 m from the wellbore, tensile fractures were primarily formed as main fractures, and were evenly expanded within the scope of fracturing. In the far-wellbore area, shear fractures formed a high-density area within the range of a 20–30 m lateral distance from the wellbore. The induced shear fractures at the tip of the main fractures could explain the multiple fractures in the far-wellbore area [21].

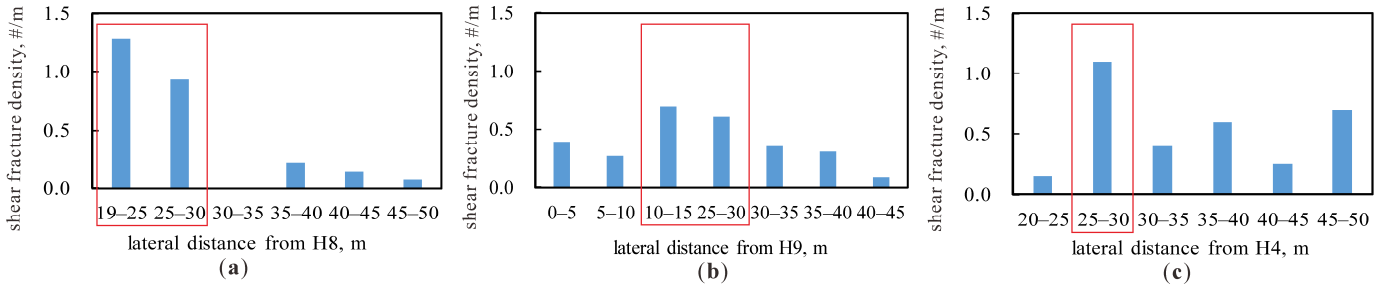



**Figure 12.** The distribution of shear fracture density with respect to the lateral distance from adjacent wells. (**a**) H8; (**b**) H9; (**c**) H4.

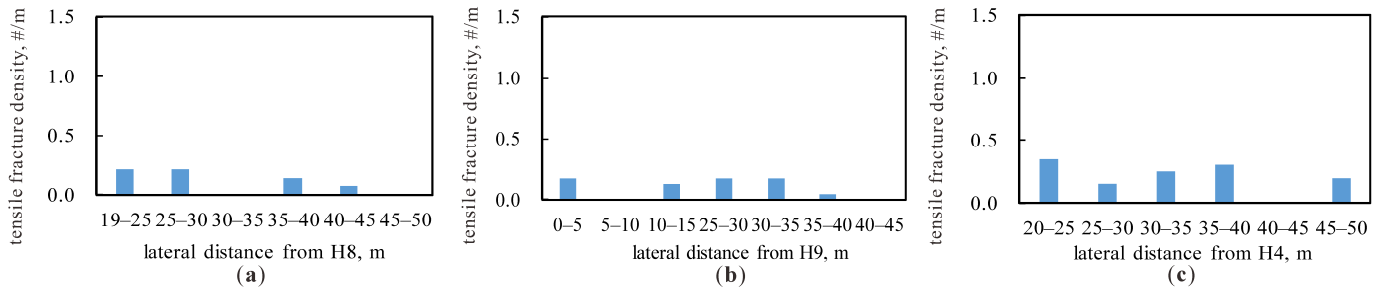



**Figure 13.** The distribution of tensile fracture density with respect to the lateral distance from adjacent wells. (**a**) H8; (**b**) H9; (**c**) H4.

As the core fracture classification and identification were based on the slant core of the CHFTS, we conducted further validation against numerical simulation to test the reasonability of the core fracture classification results. The purpose of this process was to

simulate the hydraulic fracture propagation and the stress state at the failure node, and verify whether the distributions of tensile fractures and shear fractures were consistent with those of the cores.

This process was simulated using 3DEC. The model dimension was 100 m × 100 m × 40 m. The natural weakness plane was considered. The linear density was set as 0.7 fractures per meter, which was consistent with the core fracture density, as shown in Figure 14. The injection rate was 0.3 $m^3$/min.

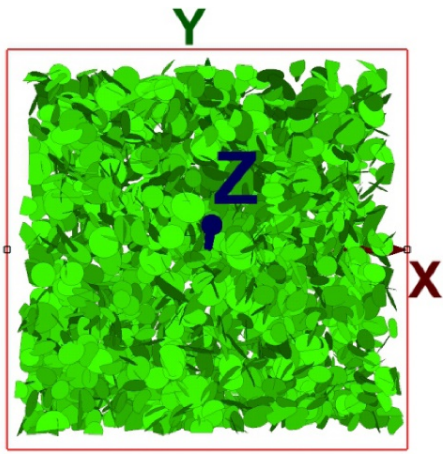



**Figure 14.** Model of the natural weakness plane.

The fracture configuration, including the distribution of fracture pore pressure and the stress state at the failure node, is illustrated in Figure 15a,b; fractures are colored according to the pore pressure and the stress state at the failure node is marked. Tensile failure nodes are shown in black, and shear failure nodes are shown in red. The results of numerical simulation were consistent with those of core fracture classification, which verified the rationality and accuracy of the core fracture classification. In the near-wellbore area less than 20–25 m from the injection point, a low stress difference and high pore pressure were more conducive to tensile failures. In the far-wellbore area, multiple shear failures were generated through interaction with the natural weak plane under a high dynamic stress difference. Eventually, multiple shear failures formed a high fracture density area within a range of approximately 20–30 m from the injection point. During hydraulic fracturing, due to a propped fracture network created close to the well, the minimum stress increased. In the pressurized zone in advance of the propped zone, the effective stresses were low. Thus, shearing happened at low effective normal stress.

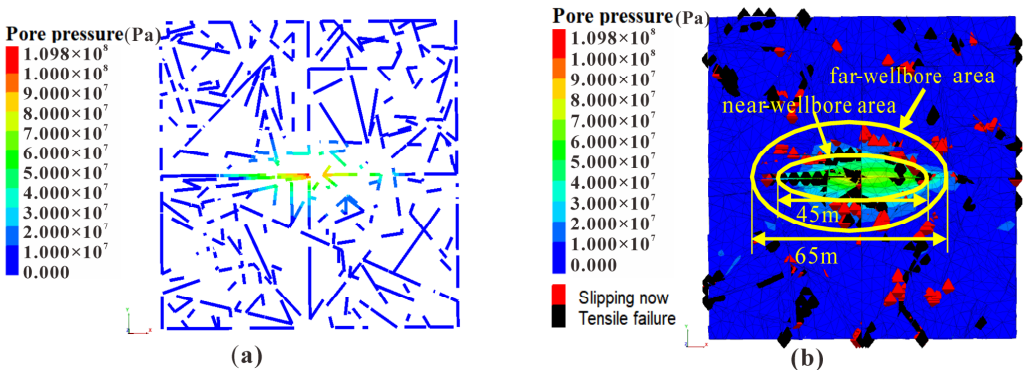



**Figure 15.** Fracture configuration after 1000 s of stimulation. (**a**) Profile of hydraulic fracture network. (**b**) Stress state at failure node. In (**a**) and (**b**), fractures are colored according to the pore pressure; tensile failure nodes are black, and shear failure nodes are red.

## 6. Conclusions

(1) The hydraulic fractures of the CHFTS were mainly linear and microwave in morphology, and the fracture surface was characterized by through-penetrating gravel and bypassing gravel patterns.
(2) According to the characteristics of the core fractures of the CHFTS, the hydraulic fractures were subdivided into tensile fractures and shear fractures. It was necessary to take the spatial distribution of tension fractures and shear fractures into consideration when obtaining the formation mechanism of hydraulic fractures.
(3) The APH–FCE method was used to identify core fracture types in the post-fracturing conglomerate reservoir, which provided good agreement with numerical simulation results.
(4) According to the fracture classification results in this study, the tensile fractures were mainly in the near-wellbore area with lateral distances of less than 20–25 m from the wellbore. The shear fractures were mainly in the far-wellbore area with lateral distances of 20–30 m from the wellbore.

**Author Contributions:** Conceptualization, R.Z. and X.M.; methodology, R.Z.; software, R.Z.; validation, J.M., Y.X. and H.S.; formal analysis, R.Z.; investigation, R.Z.; resources, X.M.; data curation, J.M.; writing—original draft preparation, R.Z.; writing—review and editing, X.M.; visualization, R.Z.; supervision, S.Z.; project administration, J.M., Y.X. and H.S. All authors have read and agreed to the published version of the manuscript.

**Funding:** This research was funded by the Xinjiang Oilfield Improvement of Shale/Tight Oil and Gas Volume Reconstruction Technology and Field Test Project (2021CGCGZ006).

**Institutional Review Board Statement:** Not applicable.

**Informed Consent Statement:** Not applicable.

**Data Availability Statement:** The raw data required to reproduce these findings cannot be shared at this time as they also form part of an ongoing study.

**Acknowledgments:** This work was supported by the Xinjiang Oilfield Improvement of Shale/Tight Oil and Gas Volume Reconstruction Technology and Field Test Project.

**Conflicts of Interest:** The authors declare no conflict of interest.

## References

1. Liu, X.; Xiong, J.; Liang, L.; You, X. Rock Mechanical Characteristics and Fracture Propagation Mechanism of Sandy Conglomerate Reservoirs in Baikouquan Formation of Mahu Sag. *Xin Jiang Pet. Geol.* **2018**, *39*, 83–91.
2. He, X.; Ma, J.; Liu, G.; Shi, S.; You, J.; Wu, J. Analysis of Rock Mechanics and Assessments of Hydraulic Fracture Network in Conglomerate Reservoirs of Mahu Oilfield. *Xin Jiang Pet. Geol.* **2019**, *40*, 701–707.
3. Li, Q.; Cheng, Y.; Ansari, U.; Han, Y.; Liu, X.; Yan, C. Experimental Investigation on Hydrate Dissociation in Near-Wellbore Region Caused by Invasion of Drilling Fluid: Ultrasonic Measurement and Analysis. *Environ. Sci. Pollut. Res.* **2022**, *29*, 36920–36937. [CrossRef] [PubMed]
4. Xv, C.; Zhang, G.; Lyu, Y.; Wang, P. Experimental study on hydraulic fracture propagation in conglomerate reservoirs. In Proceedings of the 53rd US Rock Mechanics/Geomechanics Symposium, New York, NY, USA, 23–26 June 2019.
5. Liu, P.; Ju, Y.; Ranjith, P.G.; Zheng, Z.; Chen, J. Experimental investigation of the effects of heterogeneity and geostress difference on the 3D growth and distribution of hydrofracturing cracks in unconventional reservoir rocks. *J. Nat. Gas Sci. Eng.* **2016**, *35*, 541–554. [CrossRef]
6. Yu, T.; Yuan, F.; Zhou, P.; Hao, L.; Zou, Y.; Ma, X.; Zhang, Z. Fracture Propagating Shapes in Gravel-Supported Conglomerate Reservoirs of Upper Wuerhe Formation on Manan Slope, Mahu Sag. *Xinjiang Pet. Geol.* **2021**, *42*, 53–62.
7. Dong, J.; Chen, M.; Li, Y.; Wang, S.; Zeng, C.; Zaman, M. Experimental and Theoretical Study on Dynamic Hydraulic Fracture. *Energies* **2019**, *12*, 397. [CrossRef]
8. Shentu, J.; Lin, B.; Dong, J.; Yu, H.; Shi, S.; Ma, J. Investigation of hydraulic fracture propagation in conglomerate reservoirs using discrete element method. In Proceedings of the ARMA-CUPB Geothermal International Conference, Beijing, China, 5–8 August 2019.
9. Liang, H.; Tang, H.; Qin, J.; Li, Y.; Zhou, X.; Zhang, L. Multi-Scale Investigations on the Geometries of Hydraulic Fractures in Conglomerate Reservoirs. In Proceedings of the International Petroleum Technology Conference, Riyadh, Saudi Arabia, 21–23 February 2022.

10. Katterbauer, K.; Qasim, A.; Shehri, A.A.; Zaidy, R.A. A Deep Learning Formation Image Log Classification Framework for Fracture Identification–A Study on Carbon Dioxide Injection Performancefor the New Zealand Pohokura Field. In Proceedings of the 2022 SPE Annual Technical Conference and Exhibition, Houston, TX, USA, 3–5 October 2022.
11. Udegbe, E.; Morgan, E.; Srinivasan, S. Big Data Analytics for Seismic Fracture Identification, Using Amplitude-Based Statistics. In Proceedings of the 2018 SPE Annual Technical Conference and Exhibition, Dallas, TX, USA, 24–26 September 2018.
12. Cai, H.; Zuo, H.; Wen, C.; Qian, F.; Shi, H.; Zhang, Y. Fault and Fracture identification in volcanic reservoirs: A case study from the Junggar Basin. In Proceedings of the 2017 SEG International Exposition and Annual Meeting, Houston, TX, USA, 24–29 September 2017.
13. Wang, S.; Tan, Y.; Sangnimnuan, A.; Khan, S.; Liang, B.; Rijken, P. Learnings from the Hydraulic Fracturing Test Site (HFTS) #1, Midland Basin, West Texas—A Geomechanics Perspective. In Proceedings of the Unconventional Resources Technology Conference, Denver, CO, USA, 22–24 July 2019.
14. Gale, J.F.W.; Elliott, S.J.; Li, J.Z.; Laubach, S.E. Natural Fracture Characterization in the Wolfcamp Formation at the Hydraulic Fracture Test Site (HFTS), Midland Basin, Texas. In Proceedings of the Unconventional Resources Technology Conference, Denver, CO, USA, 22–24 July 2019.
15. Vissotski, A.; Singh, A.; Rijken, P.; Reverol, R. Analysis of Completion Design Impact on Cluster Efficiency and Pressure-Based Well Communication in HFTS-2 Delaware Basin. In Proceedings of the Unconventional Resources Technology, Houston, TX, USA, 26–28 July 2021.
16. Zhang, Z.; DiSiena, J.; Bevc, D.; Ning, I.L.C.; Tan, Y.; Swafford, L.; Craven, M.; Hughes, K.; Vissotski, A. Hydraulic fracture characterization by integrating multidisciplinary data from the Hydraulic Fracturing Test Site 2 (HFTS-2). In Proceedings of the Unconventional Resources Technology Conference, Houston, TX, USA, 26–28 July 2021.
17. Gulliver, D.; Sarkar, P.; Tinker, K.; Means, N.; Fazio, J.; Xiong, W.; Hakala, A.; Lopano, C.; Leleika, S.; Harmon, A.; et al. Novel Geochemistry Determined from High Pressure, High Temperature Simulation Experiments of Hydraulic Fracture Test Site 2. In Proceedings of the Unconventional Resources Technology Conference, Houston, TX, USA, 26–28 July 2021.
18. Shi, S.; Zhuo, R.; Cheng, L.; Xiang, Y.; Ma, X.; Wang, T. Fracture Characteristics and Distribution in Slant Core from Conglomerate Hydraulic Fracturing Test Site (CHFTS) in Junggar Basin, Northwest China. *Processes* **2022**, *10*, 1646. [CrossRef]
19. Xie, D.; Guo, S.; Li, S. The Study of Green Risk Assessment for Construction Project Based on "AHP–FCE" Method. In *Modeling Risk Management in Sustainable Construction (Computational Risk Management)*; Wu, D., Ed.; Springer: Berlin, Heidelberg, 2011.
20. LI, X.; MA, X.; XIAO, F.; ZHANG, S. Combined method of candidate fracturing well in tight oil reservoirs based on fuzzy comprehensive evaluation. *Pet. Geol. Oilfield Dev. Daqing* **2022**, *41*, 147–156.
21. Weijermars, R.; Pham, T.; Stegent, N.; Dusterhoft, R. Hydraulic Fracture Propagation Paths Modeled using Time-Stepped Linear Superposition Method (TLSM): Application to Fracture Treatment Stages with Interacting Hydraulic and Natural Fractures at the Wolfcamp Field Test Site (HFTS). In Proceedings of the 54th US Rock Mechanics/Geomechanics Symposium, Golden, CO, USA, 28 June–1 July 2020.

**Disclaimer/Publisher's Note:** The statements, opinions and data contained in all publications are solely those of the individual author(s) and contributor(s) and not of MDPI and/or the editor(s). MDPI and/or the editor(s) disclaim responsibility for any injury to people or property resulting from any ideas, methods, instructions or products referred to in the content.